MAGNIF: A Tentative Lensed Rotating Disk at $z = 8.34$ detected by JWST NIRCam WFSS with Dynamical Forward Modeling

Zihao Li (黎子豪) [1], Zheng Cai [1], Fengwu Sun [2], Johan Richard [3], Maxime Trebitsch [4], Jakob M. Helton [2], Jose M. Diego [5], Masamune Oguri [6,7], Nicholas Foo [8], Xiaojing Lin [1], Franz Bauer [9,10,11], Chian-Chou Chen [12], Christopher J. Conselice [13], Daniel Espada [14,15], Eiichi Egami [2], Xiaohui Fan [2], Brenda L. Frye [2], Yoshinobu Fudamoto [16,17], Pablo G. Pérez-González [18], Kevin Hainline [2], Tiger Yu-Yang Hsiao [19], Zhiyuan Ji [2], Xiangyu Jin [2], Anton M. Koekemoer [20], Vasily Kokorev [4], Kotaro Kohno [21,22], Mingyu Li [1], Minju Lee [23,24], Georgios E. Magdis [23,24,25], Christopher N. A. Willmer [2], Rogier A. Windhorst [8], Yunjing Wu [1,2], Haojing Yan [26], Haowen Zhang (张昊文) [2], Adi Zitrin [27], Siwei Zou [1], Fuyan Bian [28], Cheng Cheng [29], Christa DeCoursey [2], Lukas J. Furtak [27], Charles Steinhardt [23,24,25], AND Hideki Umehata [30,31,32]

[1] *Department of Astronomy, Tsinghua University, Beijing 100084, China;* li-zh21@mails.tsinghua.edu.cn
[2] *Steward Observatory, University of Arizona, 933 N Cherry Avenue, Tucson, AZ 85721, USA*
[3] *Univ Lyon, Univ Lyon1, Ens de Lyon, CNRS, Centre de Recherche Astrophysique de Lyon UMR5574, F-69230, Saint-Genis-Laval, France*
[4] *Kapteyn Astronomical Institute, University of Groningen, 9700 AV Groningen, The Netherlands*
[5] *Instituto de Física de Cantabria (CSIC-UC). Avenida Los Castros s/n. E-39005 Santander, Spain*
[6] *Center for Frontier Science, Chiba University, 1-33 Yayoi-cho, Inage-ku, Chiba 263-8522, Japan*
[7] *Department of Physics, Graduate School of Science, Chiba University, 1-33 Yayoi-Cho, Inage-Ku, Chiba 263-8522, Japan*
[8] *School of Earth and Space Exploration, Arizona State University, Tempe, AZ 85287-1404, USA*
[9] *Instituto de Astrofísica and Centro de Astroingeniería, Facultad de Física, Pontificia Universidad Católica de Chile, Campus San Joaquín, Av. Vicua Mackenna 4860, Macul Santiago, 7820436, Chile*
[10] *Millennium Institute of Astrophysics, Nuncio Monseñor Sótero Sanz 100, Of 104, Providencia, Santiago, Chile*
[11] *Space Science Institute, 4750 Walnut Street, Suite 205, Boulder, Colorado 80301, USA*
[12] *Academia Sinica Institute of Astronomy and Astrophysics (ASIAA), No. 1, Sec. 4, Roosevelt Road, Taipei 10617, Taiwan*
[13] *Jodrell Bank Centre for Astrophysics, University of Manchester, Oxford Road, Manchester UK*
[14] *Departamento de Física Teórica y del Cosmos, Campus de Fuentenueva, Edificio Mecenas, Universidad de Granada, E-18071, Granada, Spain*
[15] *Instituto Carlos I de Física Teórica y Computacional, Facultad de Ciencias, E-18071, Granada, Spain*
[16] *Waseda Research Institute for Science and Engineering, Faculty of Science and Engineering, Waseda University, 3-4-1 Okubo, Shinjuku, Tokyo 169-8555, Japan*
[17] *National Astronomical Observatory of Japan, 2-21-1, Osawa, Mitaka, Tokyo, Japan*
[18] *Centro de Astrobiología (CAB), CSIC-INTA, Ctra. de Ajalvir km 4, Torrejón de Ardoz, E-28850, Madrid, Spain*
[19] *Department of Physics and Astronomy, The Johns Hopkins University, 3400 N Charles St. Baltimore, MD 21218, USA*
[20] *Space Telescope Science Institute, 3700 San Martin Dr., Baltimore, MD 21218, USA*
[21] *Institute of Astronomy, Graduate School of Science, The University of Tokyo, 2-21-1 Osawa, Mitaka, Tokyo 181-0015, Japan*
[22] *Research Center for the Early Universe, Graduate School of Science, The University of Tokyo, 7-3-1 Hongo, Bunkyo-ku, Tokyo 113-0033, Japan*
[23] *Cosmic Dawn Center (DAWN), Jagtvej 128, DK2200 Copenhagen N, Denmark*
[24] *DTU-Space, Technical University of Denmark, Elektrovej 327, DK2800 Kgs. Lyngby, Denmark*
[25] *Niels Bohr Institute, University of Copenhagen, Jagtvej 128, DK2200 Copenhagen N, Denmark*
[26] *Department of Physics and Astronomy, University of Missouri, Columbia, MO 65211, USA*
[27] *Physics Department, Ben-Gurion University of the Negev, P.O. Box 653, Be'er-Sheva 84105, Israel*
[28] *European Southern Observatory, Alonso de Cordova 3107, Casilla 19001, Vitacura, Santiago 19, Chile*
[29] *Chinese Academy of Sciences South America Center for Astronomy, National Astronomical Observatories, CAS, Beijing 100101, China*
[30] *Institute for Advanced Research, Nagoya University, Furocho, Chikusa, Nagoya 464-8602, Japan*
[31] *Department of Physics, Graduate School of Science, Nagoya University, Furocho, Chikusa, Nagoya 464-8602, Japan*
[32] *Cahill Center for Astronomy and Astrophysics, California Institute of Technology, MS 249-17, Pasadena, CA 91125, USA*

ABSTRACT

We report galaxy MACS0416-Y3 behind the lensing cluster MACSJ0416.1–2403 as a tentative rotating disk at $z = 8.34$ detected through its [O III]$\lambda 5007$ emission in JWST NIRCam wide-field slitless

spectroscopic observations. The discovery is based on our new grism dynamical modeling methodology for JWST NIRCam slitless spectroscopy, using the data from "Median-band Astrophysics with the Grism of NIRCam in Frontier Fields" (MAGNIF), a JWST Cycle-2 program. The [O III]λ5007 emission line morphology in grism data shows velocity offsets compared to the F480M direct imaging, suggestive of rotation. Assuming a geometrically thin disk model, we constrain the rotation velocity of $v_{\rm rot} = 58^{+53}_{-35}$ km s^{-1} via forward modeling of the two-dimensional (2D) spectrum. We obtain the kinematic ratio of $v_{\rm rot}/\sigma_v = 1.6^{+1.9}_{-0.9}$, where σ_v is the velocity dispersion, in line with a quasi-stable thin disk. The resulting dynamical mass is estimated to be $\log(M_{\rm dyn}/M_\odot) = 8.4^{+0.5}_{-0.7}$. If the rotation confirmed, our discovery suggests that rotating gaseous disks may have already existed within 600 million years after Big Bang.

1. INTRODUCTION

An outstanding question in galaxy evolution is the time at which galactic rotating disks are formed. In the cosmological model of Λ-Cold Dark Matter (ΛCDM), a bottom-up structure build-up is favored. Gaseous material and dark matter feed into dark matter halos through accretion or merger, allowing the structure growth (Lin et al. 1965; Zel'dovich 1970). Nevertheless, detailed physical processes dominating galaxy formation are still hotly debated. For massive galaxies, it is believed that the infalling gas is shock-heated to the virial temperature and accretes spherically before cooling and condensing into a disk that is sustained by rotation in the so called "hot mode" (Dekel & Birnboim 2006; Joung et al. 2012; Hafen et al. 2022). In this scenario, the disk of gas and stars form relatively late. In addition to "hot mode" accretion, numerical simulations predict an additional scenario in which gas efficiently accretes onto galaxies with low halo masses through flows along filamentary structures, with a sizeable portion of the gas remaining cool, at temperatures much below the virial temperature of the galaxies (Kereš et al. 2005; Ocvirk et al. 2008; Dekel et al. 2009b). In contrast to the former models, within this scenario, disk galaxies could be established at an early stage, as streams of cold gas from the intergalactic medium (IGM) could directly form a rotating disk as the gas spirals inward (Martin et al. 2016), and such cold streams are responsible for the formation of disks at high redshift (Dekel et al. 2009a). Numerical simulations show that star formation at $z > 6$ is mostly fueled by the efficient accretion of cold gas (Yajima et al. 2015), and hot mode makes negligible contribution to star formation since most of the shock-heated gas cannot cool within a Hubble time (van de Voort et al. 2011). To discriminate between these mass accretion models and learn how galaxies acquire their mass, one has to trace the earliest onset of galaxy disks (either via gas or stars, e.g., Übler et al. 2022).

Carbon monoxide (CO) or UV/optical spectroscopy at $z \approx 2.5$ has been used to identify disks (e.g., Aravena et al. 2014; Genzel et al. 2017). High angular-momentum cold-accretion on the larger scale of the circumgalactic medium (CGM) has also been identified at $z \approx 2$ (Zhang et al. 2023). Observations on CO with JVLA and [CII] with ALMA at higher redshifts of $z = 4 - 5$ have produced suggestive evidence of cold-gas disks being supported by rotation (Neeleman et al. 2020; Roman-Oliveira et al. 2023).

It is still hard to detect definitive rotating disk galaxies at $z > 5$, caused by a combination of relatively low resolution and sensitivity. Most of the successful detections from the ground were obtained by ALMA (Smit et al. 2018; Rizzo et al. 2020; Fujimoto et al. 2021; Lelli et al. 2021; Pope et al. 2023; Posses et al. 2023), but the rotation features are not always observed (Tamura et al. 2023). While it is relatively easier to detect the rotating disks among bright quasar host galaxies (Pensabene et al. 2020; Izumi et al. 2021; Neeleman et al. 2021), less massive systems are less commonly detected and often require the aid from gravitational lensing (Fujimoto et al. 2021). The most distant disk candidate so far resides at $z = 9.1$ with [O III] $88\mu m$ detected in a gravitationally lensed galaxy, MACS1149-JD1 (Hashimoto et al. 2018; Tokuoka et al. 2022).

Many hydrodynamical simulations predict ordered rotation of cold gas at redshifts as high as $z \sim 10$ (Katz et al. 2019). With the launch of JWST, there are emerging evidences that the disk galaxies are more frequent than expected by previous HST observations at redshift up to $z \sim 8$ (Ferreira et al. 2022, 2023). Such high redshift disks are expected to be detected by JWST through optical emission lines (e.g. Hα, [O III]), which trace warm/ionized gas, in complement to cold gas traced by CO or the more complex phases traced by [CII]in radio bands. The kinematics of the multi-phase ISM may

greatly help us to understand the early galaxy formation and mass assembly.

In this letter, we study the galaxy MACS0416-Y3 (Coe et al. 2015; Infante et al. 2015; Laporte et al. 2015; McLeod et al. 2015) behind the lensing cluster MACSJ0416.1–2403 and report it as a possible rotating disk at $z > 8$. The discovery is based on our methodology to forward model the kinematics of rotating disks. We find its kinematic ratio (ratio between rotation velocity and velocity dispersion) can be well predicted by semi-empirical models (Wisnioski et al. 2015), indicating a quasi-stable gas disk which has formed less than 600 Myr after the Big Bang.

The letter is organized as follows. We describe our observations and detail the data reduction procedure in Section 2. We present the lens modeling and dynamical modeling in Section 3. The kinematic results are presented in Section 4 and we conclude our findings in Section 5. Throughout this letter, we adopt the AB magnitude system (Oke & Gunn 1983), and assume a flat ΛCDM cosmology with $\Omega_m = 0.3$, $\Omega_\Lambda = 0.7$, and $H_0 = 70$ km s^{-1}Mpc^{-1}. We use the following vacuum line wavelengths: 4960.295Å for [O III]λ4959 and 5008.240Å for [O III]λ5007 based on the Atomic Line List v2.04[1].

2. OBSERVATIONS AND DATA REDUCTION

The JWST NIRCam imaging and wide field slitless spectrograph (WFSS) data were obtained through the Cycle-2 General Observer (GO) program "Median-band Astrophysics with the Grism of NIRCam in Frontier Fields" (MAGNIF; PID: 2883, PI: F. Sun). The detailed design of this program will be presented by a forthcoming paper from the collaboration. We obtained NIRCam imaging of the Frontier-Field cluster MACSJ0416.1–2403 (Lotz et al. 2017) with both the F210M and F480M filters on August 20, 2023, with total exposure time 9.3 ksec (2.58 h) and 3.2 ksec (0.89 h) in the F210M and F480M bands, respectively. we also obtained two rows of NIRCam WFSS observations with the F480M filter and the column direction grism (Grism C), each with four dithers, with total exposure time 6.2 ksec (1.72 h), and the on-source time of 3.1 ksec (0.86 h) for our target, MACS0416-Y3. All JWST data taken with this program have been made publicly available immediately on MAST[2].

2.1. Image Reduction

We reduce NIRCam imaging data with version 1.11.2 of the JWST calibration pipeline. Imaging data reduction is performed through the standard stage-1/2/3 pipeline with customized steps. We perform the so-called "snowball" masking (see Rigby et al. 2023) using the stage-1 pipeline. We subtract the "1/f" noise using the median of each row and column in stage-2. We also remove low-level background (including the "wisps") using the median-stacked image taken with each detector with proper masking of real sources. Imaging data are mosaicked in stage-3 with a pixel size of 0.″03 and `pixfrac=1`. The astrometry of mosaicked images have been registered to Gaia-DR3 (Gaia Collaboration et al. 2023).

2.2. WFSS Reduction

We use version 1.8.3 of the JWST Calibration pipeline `CALWEBB` Stage 1 to calibrate individual NIRCam WFSS exposures, with reference files `jwst_1090.pmap`. The $1/f$ noise is then subtracted along rows for our Grism-C exposures using the routine described in Wang et al. (2023). The world coordinate system (WCS) information is assigned to each exposure with `assign_wcs` step. The flat field is done with `CALWEBB` stage-2. we build the median backgrounds based on all of the MAGNIF WFSS exposures, which are then scaled and subtracted from each individual exposure. We apply an additional background subtraction, which is estimated by `photutils`(Bradley et al. 2022) to remove the residual background. We then measure the astrometric offsets between each of the short wavelength (SW) images and the fully calibrated F480M mosaic to align each grism exposure with the direct image. The correcting of this offset is important since the grism WCS should be aligned with direct image for the tracing model to work properly (c.f. Sun et al. 2023).

The pre-processed WFSS exposures are then processed by Grism Redshift & Line Analysis tool (Grizli[3]; Brammer et al. 2022). We use the spectral tracing and grism dispersion models (Sun et al. 2023) that were produced using the JWST/NIRCam commissioning data of the Large Magellanic Cloud (LMC; PID: 1076). The sensitivity models are from JWST/NIRCam Cycle-1 absolute flux calibration observations (PID: 1536/1537/1538). Both the tracing, dispersion and sensitivity [4] are converted to format accepted by Grizli. The detection catalog for spectral extraction is built from the F480M direct image, and the continuum cross-contamination is subtracted by Grizli forward model-

---

[1] https://linelist.pa.uky.edu/atomic/index.html
[2] https://mast.stsci.edu/

[3] https://github.com/gbrammer/grizli
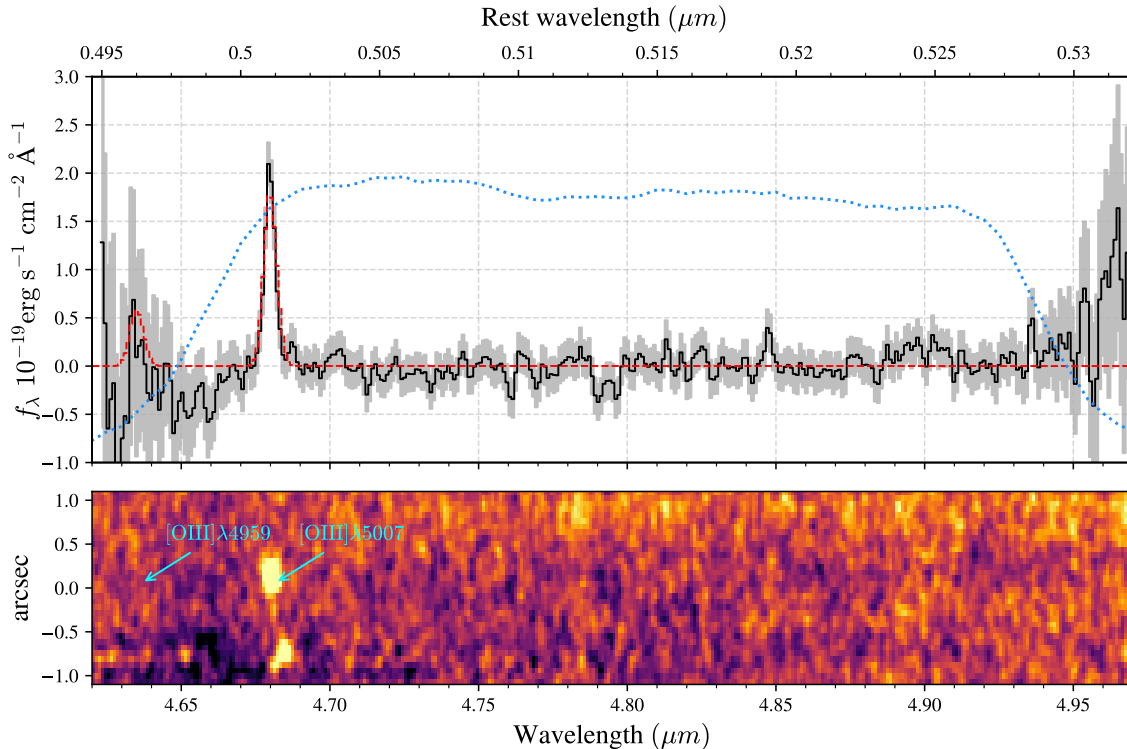[4] https://github.com/fengwusun/nircam_grism/

Figure 1. 1D (top) and 2D (bottom) spectrum of MACS0416-Y3. The red dashed line shows the best-fit model of the 1D spectrum. We overplot the F480M sensitivity as a blue dotted line to show that the [O III]λ4959 line falls out of the F480M wavelength coverage with a non-detection, while [O III]λ5007 is securely detected with SNR=16.3. We detect the other emission line ~ 1 arcsec below the center with ~ 190 km s^{-1} offset from a companion [O III] emitting galaxy of MACS0416-Y3 (the ID is MACS0416-Y2 in Laporte et al. 2015).

ing using the F480M image as the reference image for each grism exposure. The 1D spectra are extracted with optimal extraction (Horne 1986), and the emission line maps are drizzled from the 2D grism to the same WCS frame with `pixfrac=1` and pixel size=0″03, corresponding to 5 Å on the wavelength axis.

3. RESULTS AND ANALYSIS

3.1. *Lens Magnification*

We adopt the publicly available lens model of the MACSJ0416–2403 field which was constructed by Richard et al. (2021) using the `Lenstool` (Jullo et al. 2007) public software and constrained with a large number of spectroscopically confirmed multiple systems with VLT/MUSE. At this location and source redshift $z_{\rm spec} = 8.34$, the model predicts a lensing magnification factor of $\mu = 1.49$, which is consistent with the magnification computed with other publicly available lens models ($\mu \simeq 1.4 - 1.7$; e.g., Diego et al. 2015, Jauzac et al. 2015, Zitrin et al. 2015, Kawamata et al. 2016, Okabe et al. 2020), suggesting a limited uncertainty ($\lesssim 10\%$) from the lens model. While Diego et al. (in prep) suggest higher magnification $\mu = 2.2$ from the latest JWST

model, we utilize $\mu = 1.49$ for this paper to be more consistent with current models in literature. We apply the deflection map from the `Lenstool` model to reconstruct the source-plane image of MACS0416-Y3 in the F480M band, together with the corresponding `WebbPSF` (Perrin et al. 2014) model of the F480M PSF. The reconstructed image is shown in the second panel of Figure 2.

3.2. *Physical Properties of MACS0416-Y3*

The redshift of MACS0416-Y3 was previously determined as $z_{\rm phot} = 9.3^{+0.4}_{-0.5}$ (Laporte et al. 2015; see also Coe et al. 2015, McLeod et al. 2015, Infante et al. 2015, Merlin et al. 2016), this object being an HST Y_{105}-band dropout. Combining deep HST/ACS photometry (Lotz et al. 2017; Steinhardt et al. 2020) and eight-band JWST photometry at 0.8-5.0 μm from PEARLS program (Windhorst et al. 2023; N. Foo et al. in prep.), we derive a lower photometric redshift $z_{\rm phot} = 8.95^{+0.05}_{-0.14}$. The bright emission line with $\sim 16\sigma$ detection at 4.679 μm in the F480M grism data (Figure 1) is [O III]λ5007 , yielding a spectroscopic redshift for MACS0416-Y3 of $z_{\rm spec} = 8.343^{+0.002}_{-0.002}$. Solutions where this line is either [O III]λ4959 or Hβ can be easily

ruled out because the brighter [O III]λ5007 would also enter the F480M bandwidth.

We model the spectral energy distribution (SED) of MACSJ0416-Y3 using all available JWST/NIRCam photometry (N. Foo et al. in prep) with BAGPIPES (Bayesian Analysis of Galaxies for Physical Inference and Parameter EStimation; Carnall et al. 2018, 2019), adopting the default BAGPIPES stellar population models (Chevallard & Charlot 2016), which are the 2016 updated version of the models from Bruzual & Charlot (2003), assuming a Kroupa (2001) initial mass function (IMF). These models were updated to include the stellar spectral library from MILES (Falcón-Barroso et al. 2011) alongside the most recent stellar evolutionary tracks from PARSEC (Bressan et al. 2012) and COLIBRI (Marigo et al. 2013). We use the default BAGPIPES nebular emission models which are constructed following the methodology of Byler et al. (2017) using the 2017 updated version of the Cloudy photoionization code (Ferland et al. 2017). The metallicity of the ionized gas is assumed to be the same as that of the stars used to produce the ionizing photons. Finally, we assume the Calzetti et al. (2000) attenuation model. A constant star formation history (SFH) is assumed. We fix the redshift at the spectroscopic value for MACSJ0416-Y3. Log-uniform priors are assumed for the stellar mass in the range $5 < \log_{10}(M_*/M_\odot) < 13$ and the stellar age in the range $1\,\mathrm{Myr} < t_* < t_{\mathrm{univ}}$, where t_{univ} is the age of the Universe at the observed spectroscopic redshift. Uniform priors are assumed for the stellar metallicity in the range $-2.0 < \log_{10}(Z_*/Z_\odot) < +0.5$, the V-band dust attenuation in the range $0 < A_V < 8$, and the ionization parameter in the range $-4 < \log_{10}(U) < -2$.

The results of the BAGPIPES fitting suggest that MACSJ0416-Y3 is a star-forming galaxy with a stellar mass of $10^{8.6\pm0.1}\,M_\odot$ and a star-formation rate averaged over the last 10 Myr of $42\pm5\,M_\odot/\mathrm{yr}$. These values are all corrected by the lensing magnification factor $\mu = 1.49$ as described in Section 3.1. In addition, MACS0416-Y3 is found to have a young stellar population with a mass-weighted age of $5.3^{+0.5}_{-0.2}\,\mathrm{Myr}$ and moderate amounts of dust attenuation ($A_V = 1.0\pm0.1\,\mathrm{mag}$). Furthermore, we compared the BAGPIPES results to those from Prospector (Johnson et al. 2021), which provides similar functionality but differs in numerous modeling aspects. Following the methodology outlined in Tacchella et al. (2022), the results of the Prospector fitting suggest that MACS0416-Y3 is sightly less massive ($10^{8.3\pm0.1}\,M_\odot$). The two measurements are consistent within estimated errors, and we adopt BAGPIPES model, which better reproduces the observed SED with a smaller chi-square.

3.3. Dynamical Modeling

The basic method of grism dynamical modeling has been proposed by Outini & Copin (2020) and applied on HST WFC3 grism spectra. Recently, de Graaff et al. (2023) applied dynamical modeling on JWST NIRSpec MSA spectra. Here we present the technique on JWST NIRCam grism.

To obtain the dynamical modeling of the [O III]λ5007 emission of MACS0416-Y3, the procedures are summarized as follows:

1. We first fit the 2D surface brightness profile to the F480M direct image in the delensed source plane.

2. Using the derived morphological parameters, we generate the velocity field in the source plane.

3. We then map the source plane velocity information to the image plane with the lens model from Richard et al. (2021).

4. We use the F480M direct image as reference image and convolve it with the rotation velocity and velocity dispersion field from step 2 in the image plane.

5. Finally, we run Markov chain Monte Carlo (MCMC) sampling to derive the best-fit kinematic parameters and their uncertainties.

We fit a Sérsic profile convolved with the lensing reconstructed PSF to the F480M source-plane direct image using PetroFit (Geda et al. 2022).

Assuming an intrinsic circular disk, the inclination angle can be expressed as $\cos^2(i) = [(b/a)^2 - q_0^2]/(1 - q_0^2)$ (i.e., $i = 90°$ for an edge-on galaxy, see Hubble 1926), where b/a is the axis ratio of the 2D surface brightness profile, and q_0 is the intrinsic axis ratio defined by the third axis over long axis. For simplicity, we assume $q_0 = 0$. We note that the projected axis ratio can also be produced by thick disks which have been found common in high redshift $z \gtrsim 1-2$ (Zhang et al. 2019) even up to $z \sim 8$, i.e., with an observed ratio $b/a \sim 0.6$ in our case, a thick disk with $q_0 = 0.5$ would increase $\sin(i)$ by $\sim 15\%$ and influence the velocity in Eq (2). Thus, the assumption of a thin disk could lead to an rotation velocity uncertainty up to $\sim 15\%$.

We also fit the position angle of the galaxy, which is later used to determine the position of the velocity field. Figure 2 shows the best-fit results and three parameters of position angle (PA), effective radius (R_e) and inclination angle (i) are listed in Table 1.
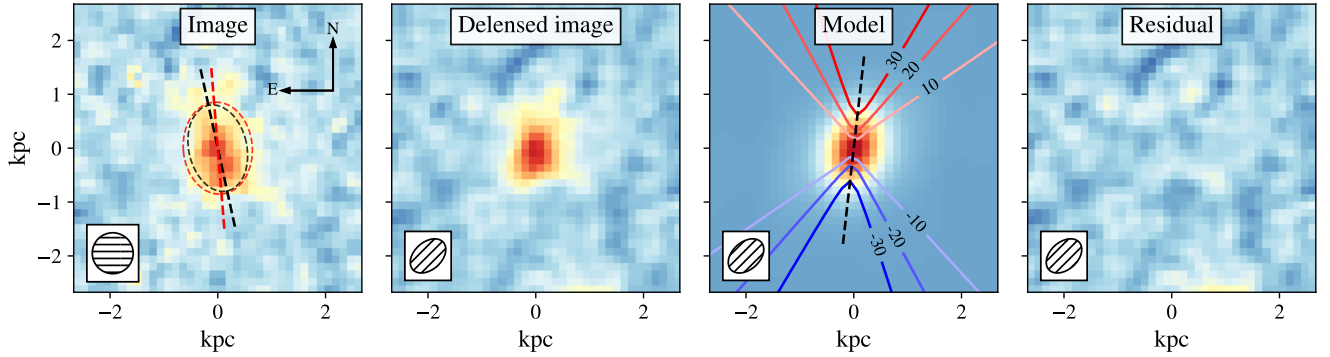
Figure 2. From left to right: the F480M direct image; reconstructed image after lensing correction; best-fit Sérsic model with PSF convolved; and the fit residuals. The original and source plane reconstructed PSFs are shown on left bottom of the corresponding panels. In the first panel, we overplot the Sérsic models of the direct image (black dashed ellipse, with black dashed line the major axis) and [O III] map (red dashed ellipse, with red dashed line the major axis) to show their spatial offset (i.e., hint of rotation) that can be directly observed. In the third panel, the contours represent the model velocity field in units of km s^{-1}, and the black dashed line is the rotation axis. The North and East orientations of all the images are indicated by the black compass in the first panel.

We use an arctangent profile model (Neeleman et al. 2020) for rotation curve parameterized as:

$$v(R) = \frac{2}{\pi} v_{\rm rot} \arctan(\frac{R}{R_v}) + v_0, \qquad (1)$$

where R is the galactocentric distance, $v_{\rm rot}$ is the maximum rotation velocity, R_v is a scaling factor determining the steepness of the rotation curve, and v_0 is the constant systemic velocity. The systemic velocity should be zero if the redshift is secured, but we keep this parameter free in our model to compensate for the small redshift uncertainty in the fitting. The line-of-sight velocity can be expressed as:

$$V_{\rm los}(x, y) = v(R) \cos(\theta) \sin(i), \qquad (2)$$

where x, y are the Cartesian coordinates in the sky plane, θ is the polar angle in the galaxy source plane, and i is the inclination angle of the galaxy. To relate the galaxy plane to the sky plane, we have that: $\tan(\theta) = \tan(\phi)/\cos(i)$, where ϕ is the polar angle in the sky plane.

The gravitational lensing distorts trajectories of photons but leaves frequencies unchanged, and the observed velocity field is also sheared (Xu et al. 2023). We convert the source plane velocity given by Eq (2) to the image plane using the deflection map obtained with the lens model, similar to that in Tokuoka et al. (2022).

We use the F480M image as the reference to model the [O III] line in the 2D grism. Since the F480M image also includes photons from the continuum and the SED modeling estimates that $\sim 57\%$ of the flux density in F480M is contributed by the [O III]$\lambda 5007$, we thus add a normalization parameter s, defined as the ratio between the [O III]$\lambda 5007$ flux and the total flux

in F480M band, to rescale the model flux. In addition, this scaling factor automatically takes the uncertainty in photometric zero points into account. An alternative way is to use a neighboring filter to subtract continuum flux from F480M, however, considering extra noise this may introduce, we apply the former.

The original F480M mosaicked image and corresponding grism [O III]$\lambda 5007$ map are aligned such that North is up and East is to the left, and we rotate the cutout by the position angle of the telescope so that the spectral dispersion direction increases towards the right. In order to conveniently model the dispersed 2D emission lines. we first convolve a 1D Gaussian kernel with a variable sigma that corresponds to the spectral resolution ($R \sim 1650$ at $4.68\,\mu m$[5]) along the wavelength direction for each row. The grism image is smoothed in a similar manner to suppress noise fluctuation below the resolution. After convolution, the image PSF is matched to the grism line spread function (LSF). Given an observed rotation velocity field, the reference image can be dispersed into the [O III]$\lambda 5007$ emission line map on the grism frame. Assuming the direct image is dominated by [O III] flux or that the [O III] is relatively smooth and follow the stellar distribution, the model emission line map can be expressed as the convolution of the direct image with the rotation velocity field. With zero velocity, the direct image can be directly transformed to the grism emission map by just changing the x coordinate unit from arcsec to wavelength (for a pixel scale=0″03 in the spatial direction, the corresponding pixel scale in wave-

[5] https://jwst-docs.stsci.edu/jwst-near-infrared-camera/nircam-instrumentation/nircam-grisms

length is 5Å). For a non-zero velocity field $V_{\rm los}(x, y)$, every pixel in the direct image at coordinate (x_0, y_0) has a wavelength offset applied:

$$\Delta\lambda(x_0, y_0) = \frac{V_{\rm los}(x_0, y_0)}{c}\lambda_{\rm obs}, \qquad (3)$$

where $\lambda_{\rm obs}$ is the observed wavelength of the [O III]$\lambda5007$ emission line in our case, and c is the speed of light. The location of each dispersed pixel is then expressed as: $(x', y') = (x_0 + \Delta\lambda/(5\text{Å}), y_0)$. We note that here we neglect the tilt of the spectral tracing, as the spatial offset in pixel dy is ~ 0.001 of the offset in wavelength direction dx (Sun et al. 2023). Given the size of the [O III]$\lambda5007$-emitting region ($dx \sim 10$), the spatial offset dy is negligible.

The shifted model is then resampled to the same pixel grid using the Cloud-in-Cell (CIC) algorithm (Birdsall & Fuss 1969) to conserve photons. To model the broadening due to the velocity dispersion, we convolve a 1-dimensional Gaussian kernel along each row with:

$$\sigma = \frac{v_\sigma}{c}\lambda_{\rm obs}, \qquad (4)$$

where v_σ is the velocity dispersion. For simplicity, we assume that v_σ is a constant over the disk.

The five free parameters in our model are rotation velocity $v_{\rm rot}$, rotation curve scaling factor R_v, systemic velocity v_0, velocity dispersion v_σ and the model scaling factor s. We keep the other parameters fixed from the Sérsic fitting previously described. We explore the model parameter space using the MCMC sampler EMCEE package (Foreman-Mackey et al. 2013). The likelihood function is defined as $L \propto \exp(-\chi^2/2)$ with:

$$\chi^2 = \sum_{x,y} \frac{(M_{\rm obs}(x, y) - M_{\rm model}(x, y))^2}{\sigma_{\rm obs}^2(x, y)}, \qquad (5)$$

where $M_{\rm obs}, M_{\rm model}$ are the observed line map and model, $\sigma_{\rm obs}$ is the uncertainty of measured surface brightness.

The prior and posterior of the MCMC sampling are discussed in Appendix A. The best-fit parameters are listed in Table 1. Figure 3 shows a comparison between the observed and best-fit [O III] line maps in the image plane. The residuals relative to background noise follow a Gaussian distribution $\mathcal{N}(-0.18, 1.06)$, with mean -0.18 and standard deviation 1.06, indicating a good fit.

One caveat is that the inferred velocity dispersion $v_\sigma = 40^{+30}_{-26}$ km s^{-1} falls below the grism velocity resolution $\sigma \approx 76$ km s^{-1}, which provides an upper limit for this parameter, and we caution the use of this value until future follow-up confirmation. Even so, our measured velocity dispersion is comparable to the typical velocity

dispersion at $z \gtrsim 6$ measured with ionized gas [O III] and Hα (de Graaff et al. 2023).

To test whether rotation is needed to reproduce the observed grism spectrum, we compare our best-fit model with a no-rotation model, the latter having zero rotation velocity while keeping other parameters the same. We find that the reduced chi-square decreases by ~ 0.1 compared to the no-rotation model, as listed in Table 1. Moreover, we applied the chi-square goodness of fit test and in the null hypothesis that the observations can be described by the model, the p-values for the chi-squares of the best-fit model and the no-rotation model are 0.02 and 0.002, respectively. Assuming a significance level of 0.01, the null hypothesis can be rejected for the no-rotation model. The solution with rotation is apparently a better fit.

Nevertheless, although our model is an excellent fit to the current data, alternative scenarios like mergers or outflows cannot be completely ruled out. A merger with two or more [O III] clumps could exhibit velocity field similar to rotation, which is challenging to be distinguished (Simons et al. 2019). Some works tried to classify major mergers and rotation disks (Shapiro et al. 2008; Rizzo et al. 2022), which usually require quantities measured at individual spaxel level in IFU datacubes to quantify certain asymmetric parameters. However, it is unpractical to extract detailed information for individual pixels in overlapped 2D spectra, and we are unable to model such complex asymmetries in our assumption of a simple rotation disk. In addition, there is a companion galaxy MACS0416-Y2 to the South of MACS0416-Y3 (see Figure 1), so we cannot rule out this as a merging system. On the other hand, the bipolar outflow or inflow could also show velocity components (e.g., Garcia-Barreto et al. 2019), while we find no obvious broad components as a sign of outflows in 1D/2D spectra in Figure 1 and there is no current evidence indicating a powerful active galactic nucleus that can power a bipolar outflow throughout the entire galaxy. Nevertheless, considering the measured rotation velocity with relatively high uncertainty $v_{\rm rot} = 58^{+53}_{-35}$ km s^{-1}, we report this system as a tentative rotating disk at the present stage. The following analysis is therefore based on the rotation assumption.

4. DISCUSSION

4.1. *A possible quasi-stable rotating disk at $z \gtrsim 8$*

In Figure 4, we compare the kinematic ratio $v_{\rm rot}/\sigma_v = 1.6^{+1.9}_{-0.9}$ from our dynamical modeling to literature observations (Neeleman et al. 2020; Lelli et al. 2021; Tokuoka et al. 2022; Roman-Oliveira et al. 2023; Fujimoto et al. 2021; de Graaff et al. 2023). We also compare the
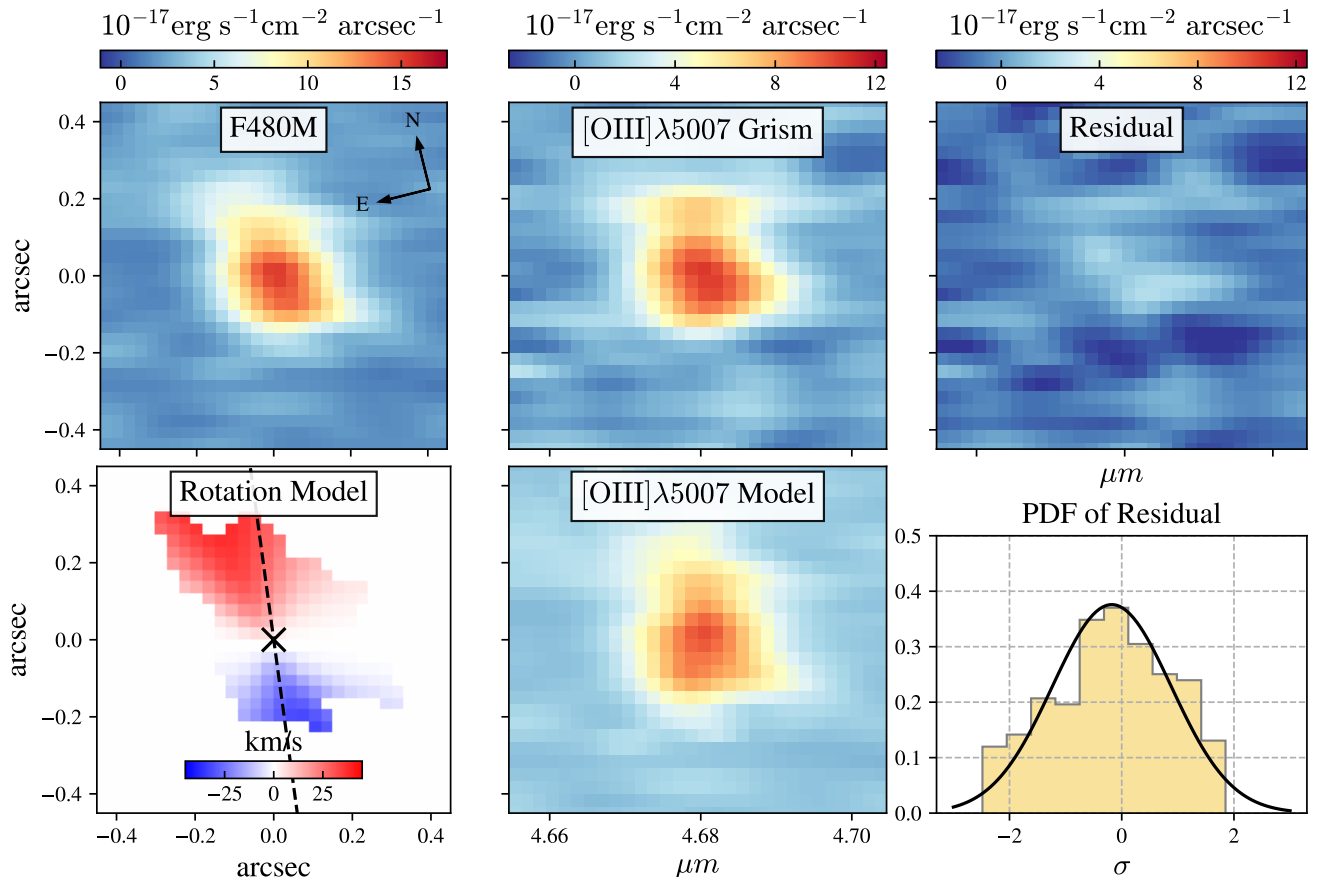
Figure 3. The first column shows the direct F480M image (top), the best-fitted rotation velocity field (bottom), with the black dashed line representing the major axis fitted in the source plane and the black × marking the model kinematic center. Second column shows the [O III]$\lambda5007$ line map (top), and the [O III]$\lambda5007$ model constructed from reference image (bottom). Both the reference image and line map are on the image plane and aligned such that the spectrum dispersion is left to right, and the North and East are annotated by the black compass. The last column shows the residual of subtracting model from [O III]$\lambda5007$ line map relative to background noise σ (top), and histogram of residuals (bottom). The residuals are well fitted by a Gaussian $\mathcal{N}(-0.18, 1.06)$, as shown in black curve.

OBELISK simulation (Trebitsch et al. 2021) to our observation. The simulated galaxies are at $z = 8.36$ with 16th and 84th percentile of stellar mass being $10^{8.4} M_\odot$ and $10^{9.3} M_\odot$. The rotation velocity is measured as the average over the galaxy of the tangential component of gas velocity, and the velocity dispersion is measured as the quadratic sum of the velocity components. Both averages are weighted by the gas density squared, as the [OIII] line emissivity. The measured kinematic ratio ranges from ~ 0.5 to ~ 3. Our observed kinematics ratio reasonably agrees with the simulation.

The redshift evolution of the kinematic ratio can be described by a semi-empirical model based on the Toomre disk instability parameter $Q_{\rm crit}$ (Wisnioski et al. 2015). This parameter, mainly parameterized with gas surface density and epicyclic frequency (Toomre 1964), determines if a differentially rotating system is stable. Disks are believed to be stable against collapse above

$Q_{\rm crit}$. We extrapolate this semi-empirical model to $z > 8$ and $\log(M_*/M_\odot) = 8$, originally fitted from a sample with $0.7 < z < 2.7$ and $9.2 < \log(M_*/M_\odot) < 11.2$. With hydrodynamical simulations, Kim & Ostriker (2007) found $Q_{\rm crit} = 0.67$ for a thick disk with gas and stars, and $Q_{\rm crit} = 1.27$ for a thin disk with gas and stars, while a thin gaseous quasi-stable disk has $Q_{\rm crit} = 1$. In Figure 4, we show this model prediction within $0.67 < Q_{\rm crit} < 1.4$, and find that our results appear consistent with semi-empirical model, in preference of a quasi-stable gaseous disk.

The gas fraction (atomic gas and molecular gas) of the disk can be estimated as: $f_{\rm gas} = M_{\rm gas}/(M_{\rm gas} + M_{\rm star}) = (a/Q_{\rm crit})(\sigma_v/v_{rot})$, where a depends on the velocity profile, e.g., $a = 1$ for a Keplerian disk and $a = 2$ for a solid-body disk (Genzel et al. 2011). Taking $Q_{\rm crit} = 1$, the modelled kinematic ratio then indicates a gas fraction $f_{\rm gas} \gtrsim 0.6$. This is consistent with high redshift

Table 1. Physical properties of MACS0416–Y3.

Property	Value
Basic Properties	
R.A. (deg)	64.048125
Dec. (deg)	-24.081452
z_{spec}	8.343 ± 0.002
$f_{\mathrm{[O\ III]}\lambda5007}$ (erg s^{-1}cm^{-2})	$(1.03 \pm 0.06) \times 10^{-17}$
μ	1.49
Morphology Properties[a]	
R_e (kpc)	0.29 ± 0.01
PA (deg)	83.6 ± 5.1
i (deg)	53.1 ± 2.3
SED Properties [b]	
$\log(M_*/M_\odot)$	$8.6^{+0.1}_{-0.1}$
SFR ($M_\odot$ yr^{-1})	42^{+5}_{-5}
Best-fit Model Parameters	
v_{rot} (km s^{-1})	58^{+53}_{-35}
v_σ (km s^{-1})	40^{+30}_{-26}
v_0 (km s^{-1})	-3^{+12}_{-12}
R_v (kpc)	$0.62^{+0.28}_{-0.27}$
s	$0.63^{+0.04}_{-0.04}$
reduced χ^2_{Best} [c]	1.18
reduced $\chi^2_{\mathrm{no-rot}}$ [c]	1.27
Derived Properties	
$v_{\mathrm{rot}}/v_\sigma$	$1.6^{+1.9}_{-0.9}$
$\log(M_{\mathrm{dyn}}/M_\odot)$	$8.4^{+0.5}_{-0.7}$

[a] Values fitted on source plane by PetroFit. The orientation of PA is defined such that right is $0°$ and up is $90°$.

[b] These values are corrected by lens magnification $\mu = 1.49$.

[c] χ^2_{Best} is calculated with our best-fit model, while $\chi^2_{\mathrm{no-rot}}$ assumes no rotation for comparison.

main sequence galaxies with high gas fraction (Aravena et al. 2020; Walter et al. 2022; Li et al. in prep). The gas fraction together with the rotation-dominated nature may indicate ongoing gas accretion, and the rotation is sustained by angular momentum from inspiraling gas (Stewart et al. 2011, 2017; Zhang et al. 2023).

4.2. Dynamical mass versus stellar mass

Assuming a spherical mass distribution, the dynamical mass at radius R can be estimated as:

$$M_{\mathrm{dyn}}/M_\odot = 2.32 \times 10^5 v(R)^2 R, \qquad (6)$$

where $v(R)$ is the rotation velocity (km s^{-1}) at radius R (kpc). We assume the extent of the galaxy to be three times the effective radius ($R_e = 0.29$ kpc) in F480M to estimate the dynamical mass, corresponding to the region enclosing $80\% - 90\%$ of the total flux density in our sérsic model, which is a reasonable choice to define galaxy size (Neeleman et al. 2020). We measure a dynamical mass $\log(M_{\mathrm{dyn}}/M_\odot) = 8.4^{+0.5}_{-0.7}$. As noted by Neeleman et al. (2020), this underestimates the dynamical mass by up to 30% for an exponential thin-disk instead of spherical mass distribution, due to their different rotation curves (Walter et al. 1997). Moreover, since the rotation velocity can be reduced in the presence of pressure gradients of turbulent gas (Burkert et al. 2010), the actual dynamical mass can be several times larger (e.g., Tokuoka et al. 2022 estimated it to be ~ 5 times larger in case of $v_{\mathrm{rot}}/v_\sigma \sim 1$). With our measured kinematic ratio $v_{\mathrm{rot}}/v_\sigma \sim 1.6$, we estimate the dynamical mass to be increased by a factor of ~ 3 (see Tokuoka et al. 2022; Burkert et al. 2010 about this correction). The corrected dynamical mass is $\log(M_{\mathrm{dyn}}/M_\odot) \sim 8.9$. Comparing to our measured stellar mass $\log(M_*/M_\odot) = 8.6^{+0.1}_{-0.1}$ (lensing corrected) and the estimated gas fraction $\gtrsim 0.6$, the corrected dynamical mass broadly agrees with the sum of stellar and gas components. As this source has a young mass-weighted age ~ 5 Myr (discussed in Section 3.2), the dynamical mass can be attributed to a young stellar population and high fraction of gas, and the uncertainties in stellar mass and dynamical mass also give room for dark matter to exist in this galaxy.

4.3. Rotating disks as a consequence of gas accretion?

The star-formation history of high redshift galaxies could be dominated by continuous or bursty star-formation, with a much higher gas fraction than today (Tacconi et al. 2020). Assuming the gas fraction $f_{\mathrm{gas}} = 0.6$ for MACS0416-Y3 as inferred in Section 4.1, the gas mass is estimated to be $M_{\mathrm{gas}} \sim 10^{8.8}\,M_\odot$. With the star formation rate $42\,M_\odot$/yr from SED fitting, this leads to a short gas depletion time $t_{\mathrm{dep}} \sim 15$ Myr. This high sSFR should be sustained by continuous gas replenishment via cold mode accretion (Dekel et al. 2009b; Kereš et al. 2009; Cresci et al. 2010), otherwise it would be quenched at $z \sim 8.19$. The cold streams tend to orbit with high angular momentum before building the galactic disk (Stewart et al. 2011; Zhang et al. 2023). In this scenario, we would expect the gas and young stars to settle into an ordered rotation. Therefore, the gas with high angular momentum in our observed disk at $z \gtrsim 8$ is possibly brought from the efficient accretion at early stage of galaxy mass assembly (Neeleman et al. 2020; Tacchella et al. 2023; Heintz et al. 2023). Further stud-
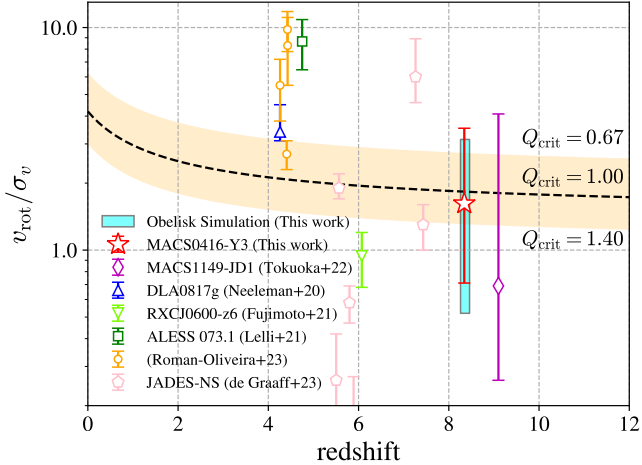
Figure 4. Kinematic ratio $v_{\rm rot}/\sigma_v$ as a function of redshift. The red star shows our result with NIRCam WFSS, and other symbols show literature observations using ALMA (Neeleman et al. 2020; Lelli et al. 2021; Tokuoka et al. 2022; Fujimoto et al. 2021; Roman-Oliveira et al. 2023) and JWST NIRSpec MSA (de Graaff et al. 2023). The cyan shadowed area represents the 1σ interval predicted by OBELISK simulation. The dashed line shows the semi-empirical models based on Toomre's disk instability parameter with $Q_{\rm crit} = 1.0$, and the shadowed area represents the interval between $Q_{\rm crit} = 0.67$ and $Q_{\rm crit} = 1.4$ (Wisnioski et al. 2015). We extrapolated the model down to a stellar mass $\log(M_*/M_\odot) = 8.6$ to compare with MACS0416-Y3.

ies are still needed to investigate the coupling between accreted gas and galaxy disks.

5. CONCLUSIONS

Through forward modeling of the JWST NIRCam grism spectra of MACS0416-Y3, we identify a possibly rotation-dominated disk at $z = 8.34$. The kinematic ratio of this galaxy is within the expectation from a semi-empirical model. We conclude that this source may have already built a quasi-stable gas disk with stellar component and ongoing star formation from cold gas. Our discovery and similar ones from the literature (Tokuoka et al. 2022) suggest that it is possible for disks to form at $z \gtrsim 8$, as predicted in some simulations like Aspen (Katz et al. 2019) and Obelisk. These findings make it viable to study the formation history of galaxies starting from the first billion years of the Universe (Xiang & Rix 2022).

Moreover, our work illustrates the possibility for JWST NIRCam WFSS to study galaxy kinematics even at $z > 8$. The forward modeling technique proposed in this letter can also be applied to galaxies with other bright optical or near infrared lines (e.g., Hα, Pα, [S III]). Given the large field of view of the NIRCam grism (up to $\sim 9\,{\rm arcmin}^2$, in contrast to $9\,{\rm arcsec}^2$ of that for NIR-

Spec integral field unit, IFU spectroscopy), we expect that a larger sample of disks can be discovered soon in other current and future WFSS surveys, e.g., AS-PIRE (Wang et al. 2023), FRESCO (Oesch et al. 2023), EIGER (Kashino et al. 2023) and so on. As an extra example, we also present the dynamic forward modeling of a luminous Hα-emitting galaxy at $z = 5.39$ in FRESCO (Nelson et al. 2023) in Appendix B, where the rotation disk can be easily modeled. The NIRCam WFSS can be a powerful tool to pre-select high-redshift galaxies with observable kinematics for future detailed follow-up studies.

This is a pathfinder study to forward modeling the JWST NIRCam WFSS emission-line spectra, and therefore the possible systematic errors are still under investigation. We note the complexity of slitless spectroscopy where the self-contamination and cross-contamination have been a long-term problem, and the spectra overlapping may impact any measurement. Results presented in this letter can be validated by future observations with JWST NIRSpec IFU observations and high-resolution ALMA imaging, with kinematics from both ionized gas with [O III]$\lambda 5007$ and relatively cooler gas with [CII].

This grism forward modeling code is under development and will be made publicly available in our future work based on a larger sample.

APPENDIX

A. MCMC SAMPLING

We apply a flat prior for the following parameters: $v_{\rm rot} \sim \mathcal{U}(0, 300)$ km s$^{-1}, v_0 \sim \mathcal{U}(-30, 30)$ kms^{-1}, $v_\sigma \sim \mathcal{U}(0, 1000)$km s^{-1} and $s \sim \mathcal{U}(0, 100)$, and we apply a Gaussian prior on R_v with $\mathcal{N}(0.5, 0.3)$ kpc. The EMCEE sampling is performed with 64 walkers, 10000 iterations each and with a burn-in period $n = 200$. The posterior probability distribution for the parameters are shown in Figure 5, with the best-fit model shown on the top right panel.

B. EXTRA EXAMPLE: A REMARKABLE ROTATING DISK IN GOODS-S FIELD

We provide an extra example of a luminous Hα emitting galaxy with significant rotation signatures at $z = 5.39$ (Ra=53.10171, Dec=-27.83617) found in FRESCO GOODS-S field (Nelson et al. 2023, Oesch et al. 2023; also see Helton et al. 2023). The FRESCO data reduction procedures are similar to Section 2. We apply the same modeling procedures in Section 3.3, except for lensing correction steps, because GOODS-S is not a lensing field. As this source has a stronger continuum, which has a strong impact on the flux distribution of the Hα model, we thus make the reference image from F444W subtracted by F210M to mitigate continuum flux. The best-fit results are shown in Figure B. We fit the rotation velocity $v_{\rm rot} = 302^{+20}_{-20}$ km s^{-1} and velocity dispersion $\sigma_v = 118^{+7}_{-7}$ km s^{-1}. This rotation velocity $v_{\rm rot}$ is the maximum velocity defined in Eq (1), and if we measure the velocity at the effective radius $R_e = 2.25$ kpc for comparison with Nelson et al. (2023), we yield $v(R_e) = 211^{+21}_{-18}$ km s^{-1}. Our measured rotation velocity and velocity dispersion are fairly consistent with Nelson et al. (2023) (see their Figure 3 and Figure 4).

REFERENCES

Aravena, M., Hodge, J. A., Wagg, J., et al. 2014, MNRAS, 442, 558, doi: 10.1093/mnras/stu838

Aravena, M., Boogaard, L., Gónzalez-López, J., et al. 2020, ApJ, 901, 79, doi: 10.3847/1538-4357/ab99a2

Astropy Collaboration, Price-Whelan, A. M., Sipőcz, B. M., et al. 2018, AJ, 156, 123, doi: 10.3847/1538-3881/aabc4f

Birdsall, C. K., & Fuss, D. 1969, Journal of Computational Physics, 3, 494, doi: 10.1016/0021-9991(69)90058-8

Bradley, L., Sipcz, B., Robitaille, T., et al. 2022, astropy/photutils: 1.5.0, 1.5.0, Zenodo, doi: 10.5281/zenodo.6825092

Brammer, G., Strait, V., Matharu, J., & Momcheva, I. 2022, grizli, 1.5.0, Zenodo, Zenodo, doi: 10.5281/zenodo.6672538

Bressan, A., Marigo, P., Girardi, L., et al. 2012, MNRAS, 427, 127, doi: 10.1111/j.1365-2966.2012.21948.x

Bruzual, G., & Charlot, S. 2003, MNRAS, 344, 1000, doi: 10.1046/j.1365-8711.2003.06897.x

Burkert, A., Genzel, R., Bouché, N., et al. 2010, ApJ, 725, 2324, doi: 10.1088/0004-637X/725/2/2324

Bushouse, H., Eisenhamer, J., Dencheva, N., et al. 2023, JWST Calibration Pipeline, 1.11.4, Zenodo, doi: 10.5281/zenodo.8247246
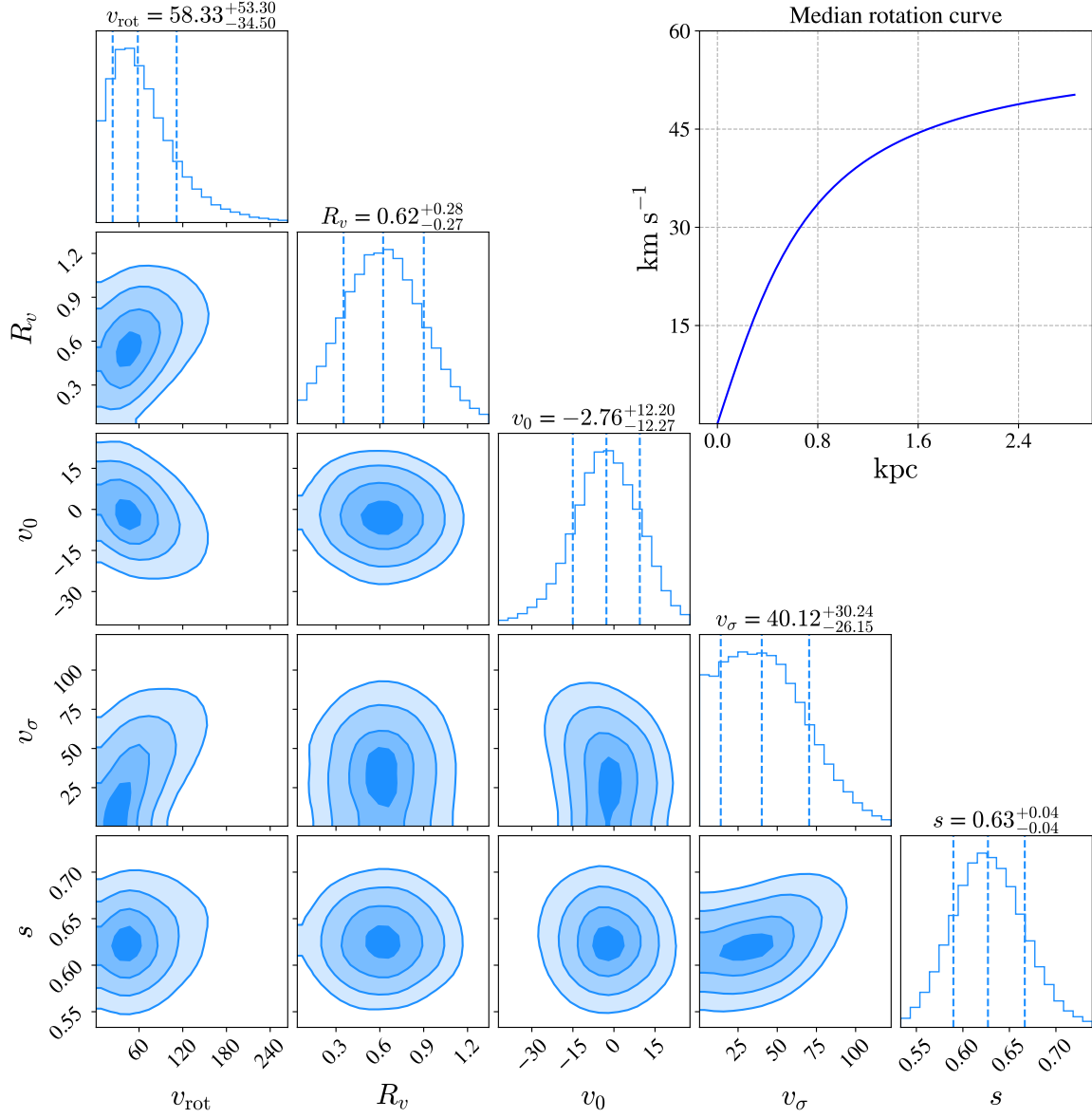
Figure 5. Posterior distribution of v_{rot}, R_v, v_0 and s in our dynamical model from MCMC sampling. The values on the top of each column are the medians with 1σ uncertainties. The top right panel shows the rotation curve with the median of each parameters.

Byler, N., Dalcanton, J. J., Conroy, C., & Johnson, B. D. 2017, ApJ, 840, 44, doi: 10.3847/1538-4357/aa6c66

Calzetti, D., Armus, L., Bohlin, R. C., et al. 2000, ApJ, 533, 682, doi: 10.1086/308692

Carnall, A. C., McLure, R. J., Dunlop, J. S., & Davé, R. 2018, MNRAS, 480, 4379, doi: 10.1093/mnras/sty2169

Carnall, A. C., McLure, R. J., Dunlop, J. S., et al. 2019, MNRAS, 490, 417, doi: 10.1093/mnras/stz2544

Chevallard, J., & Charlot, S. 2016, MNRAS, 462, 1415, doi: 10.1093/mnras/stw1756

Coe, D., Bradley, L., & Zitrin, A. 2015, ApJ, 800, 84, doi: 10.1088/0004-637X/800/2/84

Cresci, G., Mannucci, F., Maiolino, R., et al. 2010, Nature, 467, 811, doi: 10.1038/nature09451

de Graaff, A., Rix, H.-W., Carniani, S., et al. 2023, arXiv e-prints, arXiv:2308.09742, doi: 10.48550/arXiv.2308.09742

Dekel, A., & Birnboim, Y. 2006, MNRAS, 368, 2, doi: 10.1111/j.1365-2966.2006.10145.x

Dekel, A., Sari, R., & Ceverino, D. 2009a, ApJ, 703, 785, doi: 10.1088/0004-637X/703/1/785

Dekel, A., Birnboim, Y., Engel, G., et al. 2009b, Nature, 457, 451, doi: 10.1038/nature07648
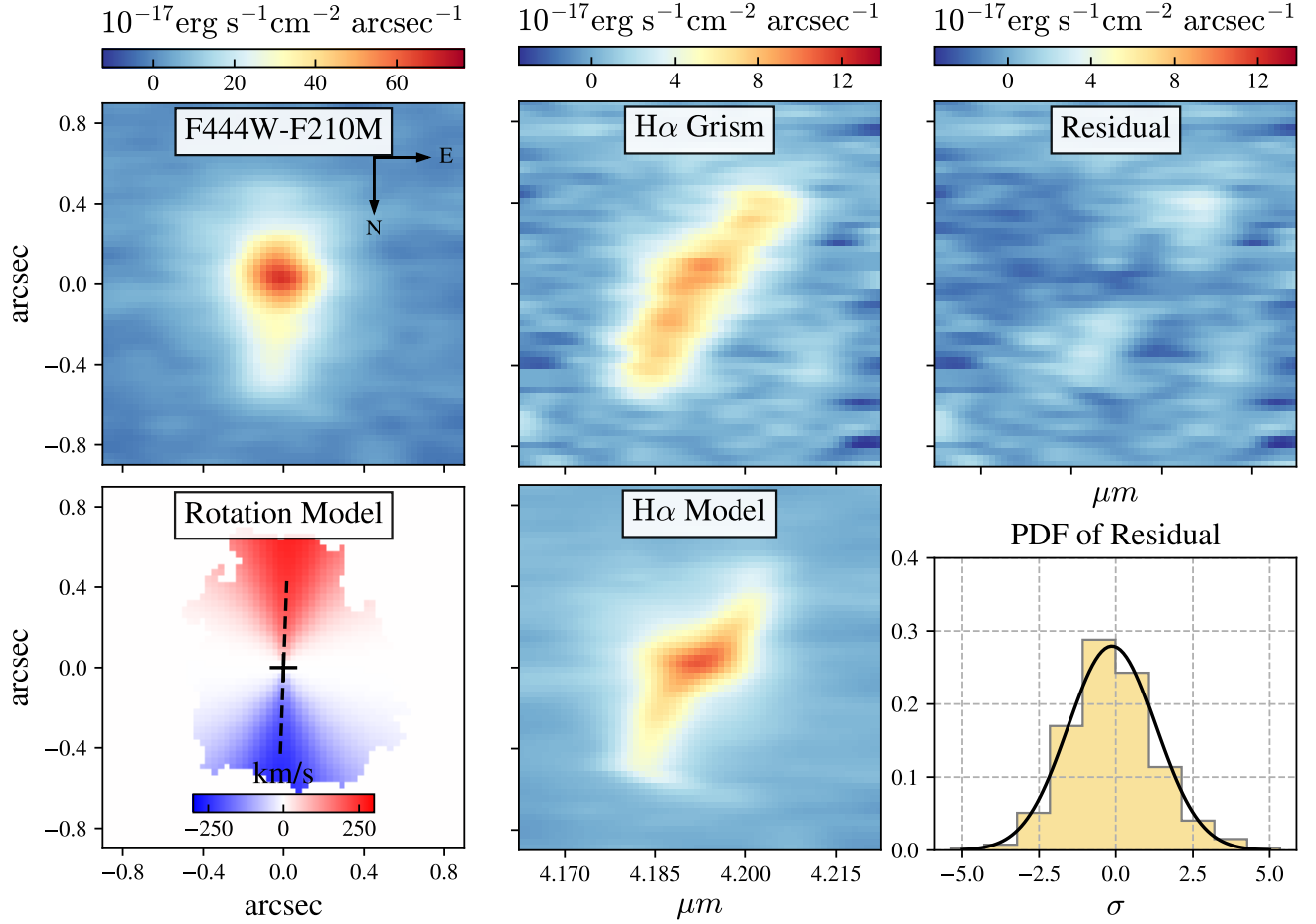
Figure 6. The same as Figure 3, but for an Hα emitting galaxy at $z = 5.39$ in FRESCO GOODS-S.

Diego, J. M., Broadhurst, T., Molnar, S. M., Lam, D., & Lim, J. 2015, MNRAS, 447, 3130, doi: 10.1093/mnras/stu2660

Falcón-Barroso, J., Sánchez-Blázquez, P., Vazdekis, A., et al. 2011, A&A, 532, A95, doi: 10.1051/0004-6361/201116842

Ferland, G. J., Chatzikos, M., Guzmán, F., et al. 2017, RMxAA, 53, 385, doi: 10.48550/arXiv.1705.10877

Ferreira, L., Adams, N., Conselice, C. J., et al. 2022, ApJL, 938, L2, doi: 10.3847/2041-8213/ac947c

Ferreira, L., Conselice, C. J., Sazonova, E., et al. 2023, ApJ, 955, 94, doi: 10.3847/1538-4357/acec76

Foreman-Mackey, D. 2016, The Journal of Open Source Software, 1, 24, doi: 10.21105/joss.00024

Foreman-Mackey, D., Hogg, D. W., Lang, D., & Goodman, J. 2013, PASP, 125, 306, doi: 10.1086/670067

Fujimoto, S., Oguri, M., Brammer, G., et al. 2021, ApJ, 911, 99, doi: 10.3847/1538-4357/abd7ec

Gaia Collaboration, Vallenari, A., Brown, A. G. A., et al. 2023, A&A, 674, A1, doi: 10.1051/0004-6361/202243940

Garcia-Barreto, J. A., Divakara Mayya, Y., & Guichard, J. 2019, PASP, 131, 094101, doi: 10.1088/1538-3873/ab28c3

Geda, R., Crawford, S. M., Hunt, L., et al. 2022, The Astronomical Journal, 163, 202, doi: 10.3847/1538-3881/ac5908

Genzel, R., Newman, S., Jones, T., et al. 2011, ApJ, 733, 101, doi: 10.1088/0004-637X/733/2/101

Genzel, R., Förster Schreiber, N. M., Übler, H., et al. 2017, Nature, 543, 397, doi: 10.1038/nature21685

Hafen, Z., Stern, J., Bullock, J., et al. 2022, Monthly Notices of the Royal Astronomical Society, 514, 5056, doi: 10.1093/mnras/stac1603

Harris, C. R., Millman, K. J., van der Walt, S. J., et al. 2020, Nature, 585, 357, doi: 10.1038/s41586-020-2649-2

Hashimoto, T., Laporte, N., Mawatari, K., et al. 2018, Nature, 557, 392, doi: 10.1038/s41586-018-0117-z

Heintz, K. E., Brammer, G. B., Giménez-Arteaga, C., et al. 2023, Nature Astronomy, doi: 10.1038/s41550-023-02078-7

Helton, J. M., Sun, F., Woodrum, C., et al. 2023, arXiv e-prints, arXiv:2302.10217, doi: 10.48550/arXiv.2302.10217

Horne, K. 1986, PASP, 98, 609, doi: 10.1086/131801

Hubble, E. P. 1926, ApJ, 64, 321, doi: 10.1086/143018

Hunter, J. D. 2007, Computing in Science and Engineering, 9, 90, doi: 10.1109/MCSE.2007.55

Infante, L., Zheng, W., Laporte, N., et al. 2015, ApJ, 815, 18, doi: 10.1088/0004-637X/815/1/18

Izumi, T., Matsuoka, Y., Fujimoto, S., et al. 2021, ApJ, 914, 36, doi: 10.3847/1538-4357/abf6dc

Jauzac, M., Jullo, E., Eckert, D., et al. 2015, MNRAS, 446, 4132, doi: 10.1093/mnras/stu2425

Johnson, B. D., Leja, J., Conroy, C., & Speagle, J. S. 2021, ApJS, 254, 22, doi: 10.3847/1538-4365/abef67

Joung, M. R., Putman, M. E., Bryan, G. L., Fernández, X., & Peek, J. E. G. 2012, ApJ, 759, 137, doi: 10.1088/0004-637X/759/2/137

Jullo, E., Kneib, J. P., Limousin, M., et al. 2007, New Journal of Physics, 9, 447, doi: 10.1088/1367-2630/9/12/447

Kashino, D., Lilly, S. J., Matthee, J., et al. 2023, ApJ, 950, 66, doi: 10.3847/1538-4357/acc588

Katz, H., Galligan, T. P., Kimm, T., et al. 2019, MNRAS, 487, 5902, doi: 10.1093/mnras/stz1672

Kawamata, R., Oguri, M., Ishigaki, M., Shimasaku, K., & Ouchi, M. 2016, ApJ, 819, 114, doi: 10.3847/0004-637X/819/2/114

Kereš, D., Katz, N., Fardal, M., Davé, R., & Weinberg, D. H. 2009, MNRAS, 395, 160, doi: 10.1111/j.1365-2966.2009.14541.x

Kereš, D., Katz, N., Weinberg, D. H., & Davé, R. 2005, MNRAS, 363, 2, doi: 10.1111/j.1365-2966.2005.09451.x

Kim, W.-T., & Ostriker, E. C. 2007, ApJ, 660, 1232, doi: 10.1086/513176

Kroupa, P. 2001, MNRAS, 322, 231, doi: 10.1046/j.1365-8711.2001.04022.x

Laporte, N., Streblyanska, A., Kim, S., et al. 2015, A&A, 575, A92, doi: 10.1051/0004-6361/201425040

Lelli, F., Di Teodoro, E. M., Fraternali, F., et al. 2021, Science, 371, 713, doi: 10.1126/science.abc1893

Lin, C. C., Mestel, L., & Shu, F. H. 1965, ApJ, 142, 1431, doi: 10.1086/148428

Lotz, J. M., Koekemoer, A., Coe, D., et al. 2017, ApJ, 837, 97, doi: 10.3847/1538-4357/837/1/97

Marigo, P., Bressan, A., Nanni, A., Girardi, L., & Pumo, M. L. 2013, MNRAS, 434, 488, doi: 10.1093/mnras/stt1034

Martin, D. C., Matuszewski, M., Morrissey, P., et al. 2016, ApJL, 824, L5, doi: 10.3847/2041-8205/824/1/L5

McLeod, D. J., McLure, R. J., Dunlop, J. S., et al. 2015, MNRAS, 450, 3032, doi: 10.1093/mnras/stv780

Merlin, E., Amorín, R., Castellano, M., et al. 2016, A&A, 590, A30, doi: 10.1051/0004-6361/201527513

Neeleman, M., Prochaska, J. X., Kanekar, N., & Rafelski, M. 2020, Nature, 581, 269, doi: 10.1038/s41586-020-2276-y

Neeleman, M., Novak, M., Venemans, B. P., et al. 2021, ApJ, 911, 141, doi: 10.3847/1538-4357/abe70f

Nelson, E. J., Brammer, G., Gimenez-Arteaga, C., et al. 2023, FRESCO: An extended, massive, rapidly rotating galaxy at z=5.3. https://arxiv.org/abs/2310.06887

Ocvirk, P., Pichon, C., & Teyssier, R. 2008, MNRAS, 390, 1326, doi: 10.1111/j.1365-2966.2008.13763.x

Oesch, P. A., Brammer, G., Naidu, R. P., et al. 2023, arXiv e-prints, arXiv:2304.02026, doi: 10.48550/arXiv.2304.02026

Okabe, T., Oguri, M., Peirani, S., et al. 2020, MNRAS, 496, 2591, doi: 10.1093/mnras/staa1479

Oke, J. B., & Gunn, J. E. 1983, ApJ, 266, 713, doi: 10.1086/160817

Outini, M., & Copin, Y. 2020, A&A, 633, A43, doi: 10.1051/0004-6361/201936318

Pensabene, A., Carniani, S., Perna, M., et al. 2020, A&A, 637, A84, doi: 10.1051/0004-6361/201936634

Perrin, M. D., Sivaramakrishnan, A., Lajoie, C.-P., et al. 2014, in Society of Photo-Optical Instrumentation Engineers (SPIE) Conference Series, Vol. 9143, Space Telescopes and Instrumentation 2014: Optical, Infrared, and Millimeter Wave, ed. J. Oschmann, Jacobus M., M. Clampin, G. G. Fazio, & H. A. MacEwen, 91433X, doi: 10.1117/12.2056689

Pope, A., McKinney, J., Kamieneski, P., et al. 2023, ApJL, 951, L46, doi: 10.3847/2041-8213/acdf5a

Posses, A. C., Aravena, M., González-López, J., et al. 2023, A&A, 669, A46, doi: 10.1051/0004-6361/202243399

Richard, J., Claeyssens, A., Lagattuta, D., et al. 2021, A&A, 646, A83, doi: 10.1051/0004-6361/202039462

Rigby, J., Perrin, M., McElwain, M., et al. 2023, PASP, 135, 048001, doi: 10.1088/1538-3873/acb293

Rizzo, F., Kohandel, M., Pallottini, A., et al. 2022, A&A, 667, A5, doi: 10.1051/0004-6361/202243582

Rizzo, F., Vegetti, S., Powell, D., et al. 2020, Nature, 584, 201, doi: 10.1038/s41586-020-2572-6

Roman-Oliveira, F., Fraternali, F., & Rizzo, F. 2023, MNRAS, 521, 1045, doi: 10.1093/mnras/stad530

Shapiro, K. L., Genzel, R., Förster Schreiber, N. M., et al. 2008, ApJ, 682, 231, doi: 10.1086/587133

Simons, R. C., Kassin, S. A., Snyder, G. F., et al. 2019, ApJ, 874, 59, doi: 10.3847/1538-4357/ab07c9

Smit, R., Bouwens, R. J., Carniani, S., et al. 2018, Nature, 553, 178, doi: 10.1038/nature24631

Steinhardt, C. L., Jauzac, M., Acebron, A., et al. 2020, ApJS, 247, 64, doi: 10.3847/1538-4365/ab75ed

Stewart, K. R., Kaufmann, T., Bullock, J. S., et al. 2011, ApJ, 738, 39, doi: 10.1088/0004-637X/738/1/39

Stewart, K. R., Maller, A. H., Oñorbe, J., et al. 2017, ApJ, 843, 47, doi: 10.3847/1538-4357/aa6dff

Sun, F., Egami, E., Pirzkal, N., et al. 2023, ApJ, 953, 53, doi: 10.3847/1538-4357/acd53c

Tacchella, S., Finkelstein, S. L., Bagley, M., et al. 2022, ApJ, 927, 170, doi: 10.3847/1538-4357/ac4cad

Tacchella, S., Johnson, B. D., Robertson, B. E., et al. 2023, MNRAS, 522, 6236, doi: 10.1093/mnras/stad1408

Tacconi, L. J., Genzel, R., & Sternberg, A. 2020, ARA&A, 58, 157, doi: 10.1146/annurev-astro-082812-141034

Tamura, Y., C. Bakx, T. J. L., Inoue, A. K., et al. 2023, ApJ, 952, 9, doi: 10.3847/1538-4357/acd637

Tokuoka, T., Inoue, A. K., Hashimoto, T., et al. 2022, ApJL, 933, L19, doi: 10.3847/2041-8213/ac7447

Toomre, A. 1964, ApJ, 139, 1217, doi: 10.1086/147861

Trebitsch, M., Dubois, Y., Volonteri, M., et al. 2021, A&A, 653, A154, doi: 10.1051/0004-6361/202037698

Übler, H., Förster Schreiber, N. M., van der Wel, A., et al. 2022, arXiv e-prints, arXiv:2210.03106, doi: 10.48550/arXiv.2210.03106

van de Voort, F., Schaye, J., Booth, C. M., & Dalla Vecchia, C. 2011, MNRAS, 415, 2782, doi: 10.1111/j.1365-2966.2011.18896.x

Virtanen, P., Gommers, R., Oliphant, T. E., et al. 2020, Nature Methods, 17, 261, doi: 10.1038/s41592-019-0686-2

Walter, F., Brinks, E., Duric, N., & Klein, U. 1997, AJ, 113, 2031, doi: 10.1086/118415

Walter, F., Neeleman, M., Decarli, R., et al. 2022, ApJ, 927, 21, doi: 10.3847/1538-4357/ac49e8

Wang, F., Yang, J., Hennawi, J. F., et al. 2023, ApJL, 951, L4, doi: 10.3847/2041-8213/accd6f

Windhorst, R. A., Cohen, S. H., Jansen, R. A., et al. 2023, AJ, 165, 13, doi: 10.3847/1538-3881/aca163

Wisnioski, E., Förster Schreiber, N. M., Wuyts, S., et al. 2015, ApJ, 799, 209, doi: 10.1088/0004-637X/799/2/209

Xiang, M., & Rix, H.-W. 2022, Nature, 603, 599, doi: 10.1038/s41586-022-04496-5

Xu, J., Eifler, T., Huff, E., et al. 2023, MNRAS, 519, 2535, doi: 10.1093/mnras/stac3685

Yajima, H., Li, Y., Zhu, Q., & Abel, T. 2015, ApJ, 801, 52, doi: 10.1088/0004-637X/801/1/52

Zel'dovich, Y. B. 1970, A&A, 5, 84

Zhang, H., Primack, J. R., Faber, S. M., et al. 2019, MNRAS, 484, 5170, doi: 10.1093/mnras/stz339

Zhang, S., Cai, Z., Xu, D., et al. 2023, Science, 380, 494, doi: 10.1126/science.abj9192

Zitrin, A., Fabris, A., Merten, J., et al. 2015, ApJ, 801, 44, doi: 10.1088/0004-637X/801/1/44